Journal of Power Sources 196 (2011) 9689–9695

Contents lists available at ScienceDirect

Journal of Power Sources

journal homepage: www.elsevier.com/locate/jpowsour

Nanocrystalline $Ti_{2/3}Sn_{1/3}O_2$ as anode material for Li-ion batteries

Ibrahim Issac[a], Marco Scheuermann[a], Sebastian M. Becker[a], Elisa Gil Bardají[a], Christel Adelhelm[b], Di Wang[a], Christian Kübel[a], Sylvio Indris[a,*]

[a] Institute of Nanotechnology, Karlsruhe Institute of Technology, P.O. Box 3640, 76021 Karlsruhe, Germany
[b] Institute of Applied Materials (IAM-AWP), Karlsruhe Institute of Technology, P.O. Box 3640, 76021 Karlsruhe, Germany

ARTICLE INFO

Article history:
Received 26 April 2011
Received in revised form 11 July 2011
Accepted 13 July 2011
Available online 23 July 2011

Keywords:
Lithium-ion batteries
Anode
Titanium tin oxide

ABSTRACT

We prepared nanocrystalline $Ti_{2/3}Sn_{1/3}O_2$ by a coprecipitation method starting from Ti(isopropoxide)$_4$ and $SnCl_4{\cdot}5H_2O$ followed by calcination at 600 °C. TEM and XRD measurements reveal crystallite sizes of about 5 nm and a crystal structure equivalent to those of TiO_2 rutile and SnO_2 cassiterite. The local structure was investigated with ^{119}Sn NMR and Sn Mössbauer spectroscopy. The material was cycled with *C*/20 at voltages between 3.0 and 0.02 V against Li metal. Specific capacities of 300 mAh g^{-1} were obtained for 100 cycles with voltage profiles very similar to those of pure SnO_2. Faster cycling leads to strong decrease of the capacities but after returning to *C*/20 the initial values are obtained.

1. Introduction

The future development of mobile electronic devices and electric vehicles is strongly interrelated with the improvement of Li-ion batteries [1–4]. Main focus is on the electrode materials, which should be capable of reversibly inserting large amounts of Li even at high rates. One example for an extensively studied material is SnO_2, where Li insertion takes place according to the following reactions [5,6]:

$$4Li^+ + 4e^- + SnO_2 \rightarrow 2Li_2O + Sn, \quad (1)$$

$$4.4Li^+ + 4.4e^- + Sn \rightarrow Li_{4.4}Sn. \quad (2)$$

The second part of this mechanism consists of several steps, during which different Li–Sn alloys are formed [5,7], with the final composition $Li_{4.4}Sn$. This alloy formation is accompanied by strong volume changes, resulting in mechanical stress and loss of contact to the current collector and thus to strong capacity fading. Different strategies have been pursued to cope with this problem, including the preparation of nanostructured samples [8–16], doping with Al [17] or Co [18], the use of ternary compounds [19–28], and the fabrication of nano-composites [29,30].

Another extensively studied material is TiO_2, including the polymorphs anatase [31–35], rutile [36–38], and TiO_2-B [39–41]. Here insertion of Li is based on the reaction

$$xLi^+ + xe^- + TiO_2 \rightarrow Li_xTiO_2 \quad (0 \leq x \leq 1). \quad (3)$$

It takes place at voltages of about 1.8 V, 1.5 V, and 1.6 V against Li|Li$^+$ for anatase, rutile, and TiO_2-B, respectively. For the anatase, doping with Sn has also been reported [42].

In this paper we report on electrochemical insertion of Li into a nanocrystalline solid solution of $Ti_{2/3}Sn_{1/3}O_2$. It is prepared by a coprecipitation method which offers the advantages of low cost and facile up-scaling. The particle sizes and shapes were studied by X-ray diffraction (XRD) and transmission electron microscopy (TEM). The existence of the solid solution was verified by XRD, scanning transmission electron microscopy (STEM) in combination with energy dispersive X-ray analysis (EDX), and ^{119}Sn nuclear magnetic resonance (NMR) spectroscopy. The local structure around the Sn ions was additionally studied by Sn Mössbauer spectroscopy. The electrochemical performance was investigated by galvanostatic cycling against a Li metal counter electrode in the voltage range from 2.8 V to 0.02 V.

Earlier battery tests on solids solutions of $Ti_ySn_{1-y}O_2$ ($y = 0 \ldots 1$) had been performed in the voltage range between 3 V and 1 V [28], i.e. the range where the $Ti^{4+/3+}$ reduction/oxidation occurs. Accordingly, only small amounts of Li could be inserted/removed (about 0.2 per formula unit) and the high reduction potential is disadvantageous.

2. Experimental

All educt materials were of analytical grade and were used without further purification: Ti(isopropoxide)$_4$ (Aldrich, 99.99%), $SnCl_4{\cdot}5H_2O$ (Aldrich, 98%), NaOH (Aldrich, 99.998%), and ethanol (Merck, 99.8%). A stoichiometric amount of Ti(isopropoxide)$_4$ was added dropwise to the stirring aqueous solution of $SnCl_4{\cdot}5H_2O$

* Corresponding author. Tel.: +49 721 608 28312; fax: +49 721 608 26368.
E-mail address: sylvio.indris@kit.edu (S. Indris).

0378-7753/$ – see front matter © 2011 Elsevier B.V. All rights reserved.
doi:10.1016/j.jpowsour.2011.07.046

resulting in the formation of a white colloid. Then the mixture was made basic to a pH of about 10 by dropwise addition of NaOH solution over a period of 1 h. Afterwards the temperature of the reaction mixture was increased to 60 °C on a hot plate and left stirring for about 2 h. Then the sample was filtered, washed with deionised water and ethanol, and left to dry overnight at room temperature (yield of ca. 80% of fine white powder). The sample was further dried in the oven at 100 °C for 4 h and then calcinated at 600 °C for 4 h in air. The reaction can be represented by the following equations:

$$(1/3)SnCl_4 + (2/3)Ti(OCH(CH_3)_2)_4 + 4NaOH \rightarrow Ti_{2/3}Sn_{1/3}(OH)_4 + (4/3)NaCl + (8/3)NaOCH(CH_3)_2, \quad (4)$$

$$Ti_{2/3}Sn_{1/3}(OH)_4 \xrightarrow{600\,^{\circ}C} Ti_{2/3}Sn_{1/3}O_2 + 2H_2O. \quad (5)$$

Chemical analysis was performed by different analytical methods. Oxygen was determined by carrier gas hot extraction, also known as inert gas fusion method (LECO TC 600). Tin capsules and platinum pieces (10 times of the sample weight) with low oxygen content served as fusion aid. The oxygen analysis was calibrated by TiO_2 (99.995% purity, dried at 600 °C). The calibration range was close to the composition of the sample. Carbon and sulphur determination was performed by combustion in oxygen with a W/Sn accelerator forming CO_2 and SO_2 measured by infrared detectors (LECO CS 600). Dried $CaCO_3$ and Li_2SO_4 of highest purity were used as calibration samples. The Sn and Ti content were determined by X-ray fluorescence. Analysis and calibration samples were fused in a mixture of $Li_2B_4O_7$, $LiBO_2$ and $Sr(NO_3)_2$ to form a homogeneous bead. Mixtures of dried TiO_2 and SnO_2 (99.993%, 800 °C), close to the sample's composition, were used as calibration substances and the intensities of the Ti-Kα and Sn-Lα lines were measured on an S4 Pioneer (Bruker-AXS) X-ray fluorescence spectrometer. The sodium impurity was determined by inductively coupled plasma optical emission spectroscopy (ICP-OES, Perkin Elmer OPTIMA 4300 DV) after sample digestion in hydrochloric and hydrofluoric acid.

Simultaneous TG-DSC-MS measurements were performed under Ar atmosphere on a Sensys Evo TG-DSC instrument (Setaram, France) with a heating rate of 5 °C min^{-1} from 25 °C to 600 °C using alumina crucibles. It was connected to an Omnistar mass spectrometer (Pfeiffer, Germany) for analysis of the evolved gases.

XRD was carried out on a Philips PANalytical X'Pert diffractometer (Cu $K\alpha_1$ radiation, Nickel monochromator, Bragg-Brentano geometry). The synthesized sample was investigated by TEM, STEM, and EDX in an aberration corrected FEI Titan 80–300 electron microscope operated at 300 kV accelerating voltage.

^{119}Sn MAS NMR spectra were acquired on a Bruker Avance 500 spectrometer with 2.5 mm rotors at a spinning speed of 35 kHz. The magnetic field was 11.7 T corresponding to a resonance frequency of 186.5 MHz. A rotor-synchronized hahn-echo pulse sequence was used with a $\pi/2$ pulse length of 2.2 μs and a recycle delay of 60 s. Spectra were referenced to microcrystalline SnO_2 with an isotropic chemical shift of −604.3 ppm [43,44].

^{119}Sn Mössbauer spectroscopic measurements were carried out in transmission mode at room temperature (drive unit from Wissel electronics, detector from LND). ^{119}Sn-enriched $CaSnO_3$ (Ainsley Technologies) was used as a γ-ray source. The velocity scale was calibrated with SnO powder which has an isomer shift of 2.63 mm s^{-1} and a quadrupole splitting of 1.30 mm s^{-1} [45,46]. For each sample 10 mg of powder was deposited on an area of 1 cm^2.

Electrochemical tests were performed in coin-cell batteries using lithium foil as counter electrode. Cells were assembled in an argon-filled glove box. The electrode films were prepared from a mixture of 80% active material, 10% polyvinyl diene fluoride (Arkema Inc.), and 10% carbon black (Super P, Timcal). Drying of the films was done at 90 °C for 12 h. Typical mass load was 1 mg cm^{-2} and typical film thickness was 50 μm. The electrolyte was 1 M $LiPF_6$ in ethylene carbonate/dimethyl carbonate (1:1 weight ratio, Ferro Fine Chemicals). The cells were galvanostatically cycled using a VMP3 galvanostat (Biologic).

3. Results and discussion

The chemical analysis of the as-prepared sample yields the composition listed in Table 1. The errors were calculated from the bias of the calibration function. The results are consistent with a composition of $Ti_{2/3}Sn_{1/3}O_2$ together with sodium containing impurities.

Thermogravimetric-differential scanning calorimetry in combination with mass spectrometry (TG-DSC-MS) was used to determine the calcination temperature required to remove water and other decomposable organic materials present during the preparation process. It was also used to suggest the correct formula for the decomposition reaction of the as-prepared precursor, in combination with elemental analysis of the material calcinated at 600 °C for 4 h, and to observe any phase changes or decomposition.

The TG curve of the as-prepared sample (Fig. 1) reveals that the dehydration process of the precursor starts at about 100 °C and is finished at about 440 °C. This is confirmed by the MS signals for mass 17 (OH) and 18 (H_2O). The dTG curve shows two steps of dehydration processes, the first one with a maximum at 160 °C and the second with a maximum at 300 °C. The overall weight loss is about 9%. No significant weight loss was observed beyond 400 °C. The DSC curve exhibits two endothermic peaks. The first broad peak with a maximum at about 150 °C corresponds to the dehydration process. The second sharp and intense peak located at 560 °C may be attributed to the formation of a solid solution (see Eq. (5)) since there is no weight loss observed from the TG in this temperature region. The XRD pattern of the sample after this heat treatment is shown in Fig. 2. It reveals that the structure is equivalent to those of SnO_2 cassiterite and TiO_2 rutile. The very broad peaks indicate very small crystallite sizes. Using the Scherer equation [47], an average particle size of 7 nm can be estimated from the peak widths. The position of the maxima is in between the values of the database entries of the binary compounds. Two explanations are possible. First, a solid solution would result in lattice constants in between those of the binary compounds. Second, a mixture of SnO_2 and TiO_2 nanocrystals would result in broad peaks at the positions of the binary compounds, but superposition again would lead to maxima at positions in between those of the binary compounds.

Fig. 3 shows the overview TEM micrograph with the selected area electron diffraction (SAED) pattern in the inset. In the thin area, the interface between particles could be reasonably distinguished and the particle size was estimated to be around 5 nm, in good agreement with XRD results. The lattice spacings of the main diffraction were measured from SAED pattern and listed in Table 2. They are slightly smaller than the lattice spacings of SnO_2 measured by XRD. Fig. 4 shows the high-resolution TEM (HRTEM) image of many particles, together with the fast Fourier transform (FFT) of the image. The rings in the FFT represent the lattice spacings present in the HRTEM image. The measured lattice spacings are also listed in Table 2. They are in good agreement with the val-

Table 1
Chemical composition of the $Ti_{2/3}Sn_{1/3}O_2$ sample according to elemental analysis.

	Mass%
Ti	27.62 ± 0.15
Sn	31.46 ± 0.36
Ni	<0.2
S	<0.05
O	32.7 ± 0.9
Na	7.2 ± 0.2
C	0.7 ± 0.05

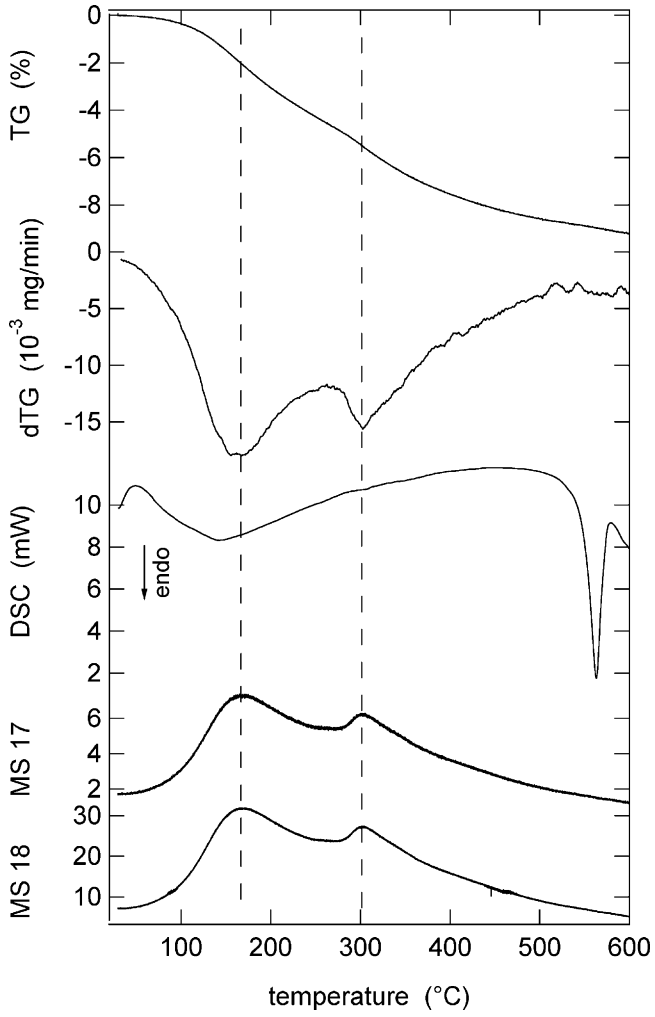

Fig. 1. Weight loss (TG), differential weight loss (dTG), differential scanning calorimetry (DSC), and MS signals of $Ti_{2/3}Sn_{1/3}O_2$.

ues measured from SAED pattern. The slight difference is due to the different calibration in diffraction and in TEM modes. Therefore the structure of $Ti_{2/3}Sn_{1/3}O_2$ nanocrystals is close to tetragonal SnO_2 but with slightly smaller lattice parameters. No separate diffraction from TiO_2 and SnO_2 was distinguished.

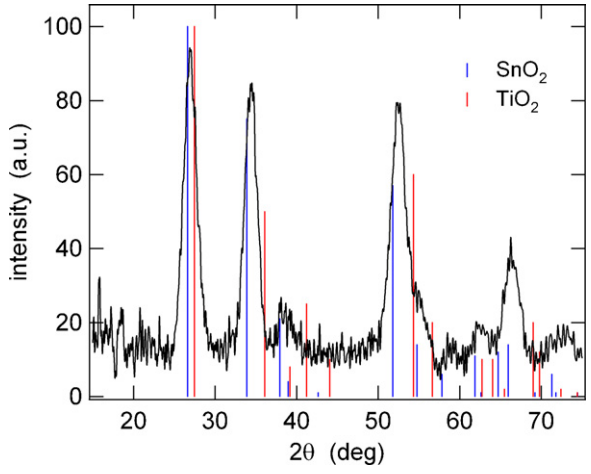

Fig. 2. XRD pattern of $Ti_{2/3}Sn_{1/3}O_2$ in comparison to database values for SnO_2 cassiterite (JCPDS 41-1445) and TiO_2 rutile (JCPDS 21-1276).

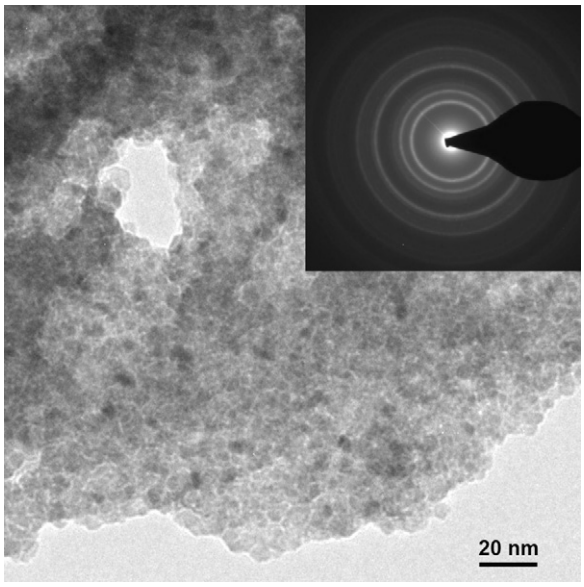

Fig. 3. Overview TEM micrograph of $Ti_{2/3}Sn_{1/3}O_2$ with the SAED pattern in the inset.

Table 2
Lattice spacings measured from SAED and HRTEM in comparison to those of SnO_2 and TiO_2.

Lattice spacings measured from SAED (Å)	Lattice spacings measured from HRTEM (Å)	SnO_2 (Å)	TiO_2 (Å)	*h k l*
3.35	3.33	3.35	3.25	1 1 0
2.64	2.62	2.64	2.49	1 0 1
2.31	2.30	2.37	2.30	2 0 0
2.15	2.11	2.12	2.05	2 1 0
1.75	1.74	1.76	1.68	2 1 1

In order to investigate the composition of the $Ti_{2/3}Sn_{1/3}O_2$ nanocrystals, EDX spectrum profiles were acquired in STEM mode, in which the electron beam is converged to the probe of about 1 nm in size so that the local composition can be characterized. Fig. 5a and b show such an EDX line profile and the results of raw quantification, respectively. The ratio of Ti:Sn fluctuates considerably along

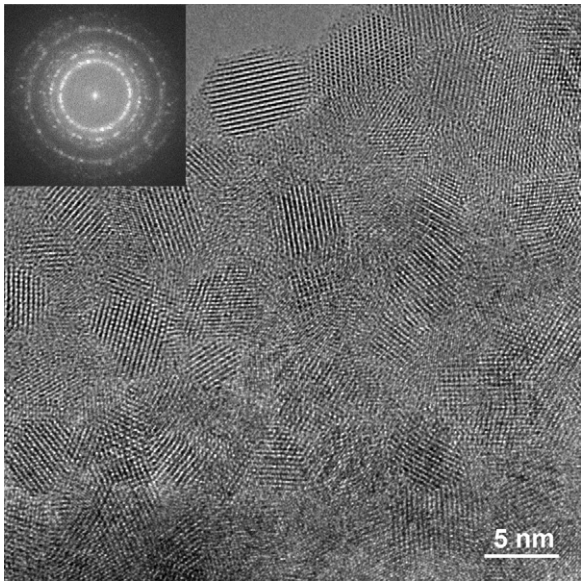

Fig. 4. HRTEM image of $Ti_{2/3}Sn_{1/3}O_2$ nanocrystals with the FFT in the inset.

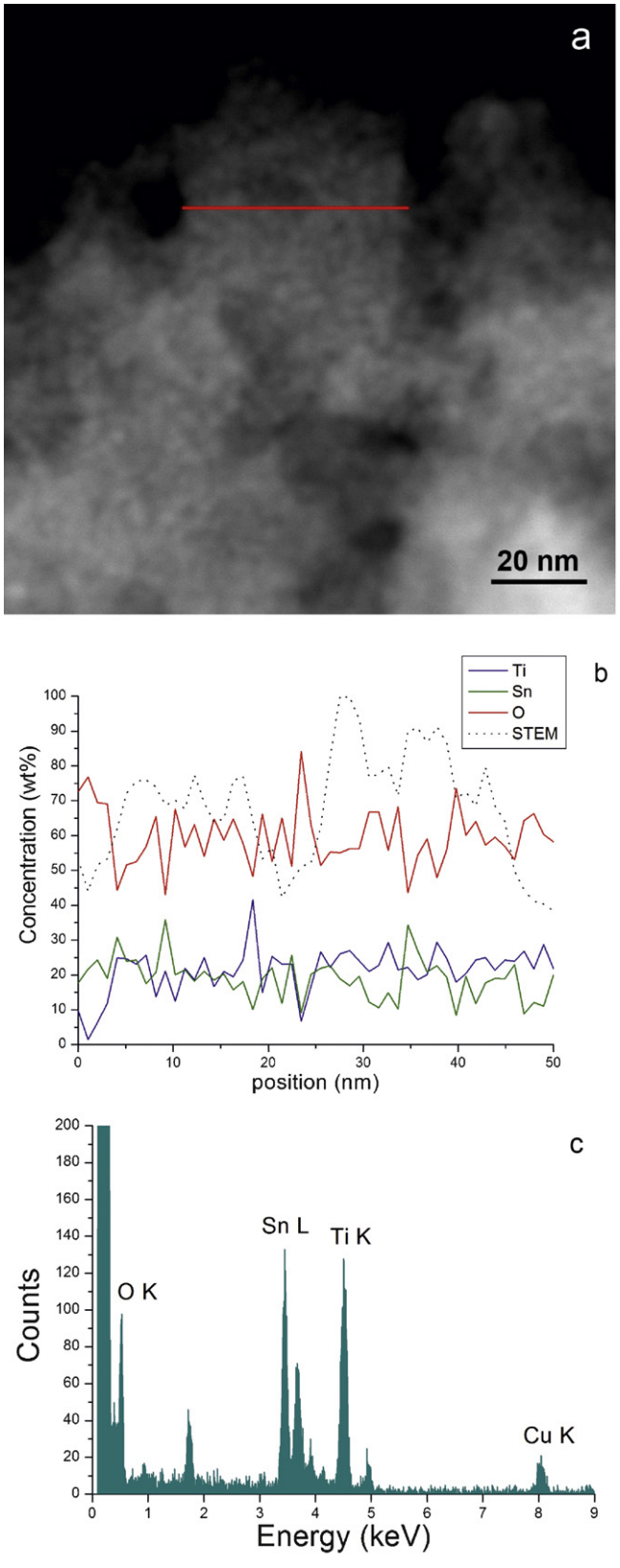

Fig. 5. (a) STEM image of $Ti_{2/3}Sn_{1/3}O_2$ with line profile indicated by a red line, along which EDX spectra were acquired on 50 positions in a total length of 50 nm; (b) the concentration profiles of Ti, Sn and O, and (c) the integrated EDX spectrum. (For interpretation of the references to color in this figure legend, the reader is referred to the web version of the article.)

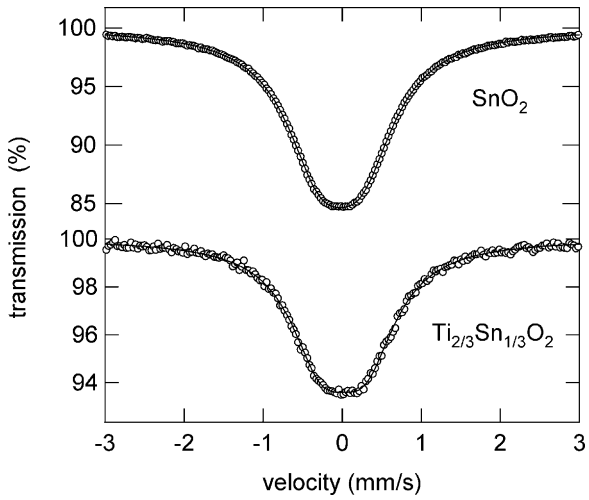

Fig. 6. Sn Mössbauer spectra of $Ti_{2/3}Sn_{1/3}O_2$ and SnO_2.

the line profile. The integrated EDX spectrum along the whole line profile is shown in Fig. 5c. The quantification using Ti K and Sn L excitations of the integrated EDX spectrum suggests an atomic ratio of Ti:Sn = 60.9:39.1. However, the EDX spectra from other areas or scanned lines also exhibit certain fluctuations of Ti:Sn ratio.

Therefore, the nanocrystals are mostly Ti–Sn mixed oxide. The crystal structure is rather uniform, which is close to the tetragonal SnO_2. The concentration of Ti and Sn varies considerably for different particles and areas.

The Mössbauer spectra of $Ti_{2/3}Sn_{1/3}O_2$ and SnO_2 are shown in Fig. 6. They have to be described in terms of a doublet with overlapping Lorentzian lines. The parameters that result from the corresponding fit (solid lines in Fig. 6) are listed in Table 3. The differences are small but significant. The bigger isomer shift found for the $Ti_{2/3}Sn_{1/3}O_2$ sample indicates a smaller average electron density at the sites of the Sn nuclei in comparison to the SnO_2 sample. The bigger quadrupole splitting for the $Ti_{2/3}Sn_{1/3}O_2$ sample reveals a bigger asymmetry around the Sn nuclei which might be caused by a solid solution of Sn and Ti on the cation sites and thus a variation of next nearest neighbours around the Sn.

Fig. 7 shows the ^{119}Sn MAS NMR spectra of $Ti_{2/3}Sn_{1/3}O_2$ and SnO_2. The spectrum of SnO_2 is characterized by a single narrow peak at −604 ppm which represents the uniform SnO_6 octahedra in the tetragonal structure of SnO_2. In contrast to that, the spectrum of $Ti_{2/3}Sn_{1/3}O_2$ reveals three contributions. A broad peak at around −604 ppm represents environments similar to those found in SnO_2. Additional peaks at around −570 ppm and −640 ppm and the fact that all peaks are very broad hint at disordered environments with Ti next nearest neighbours and thus to a solid solution. In summary, the TEM, Mössbauer, and NMR results show that the material consists of crystallites, where each crystallite is a solid solution, but where the stoichiometry of the crystallites varies slightly.

Fig. 8 shows the voltage profile for the first three cycles of galvanostatic cycling of $Ti_{2/3}Sn_{1/3}O_2$ against Li metal. A rate of C/20 was used, i.e. insertion/removal of 2 Li ions per formula unit $Ti_{2/3}Sn_{1/3}O_2$ within 20 h. The 2 Li ions per formula unit refer to the practical reversible capacity that was obtained at a very small current rate

Table 3
Mössbauer parameters of $Ti_{2/3}Sn_{1/3}O_2$ and SnO_2. All values are given in mm s^{-1}.

	Isomer shift	Quadrupole splitting	Line width
SnO_2	−0.0233 ± 0.0003	0.527 ± 0.001	1.053 ± 0.002
$Ti_{2/3}Sn_{1/3}O_2$	0.012 ± 0.002	0.553 ± 0.006	0.968 ± 0.009

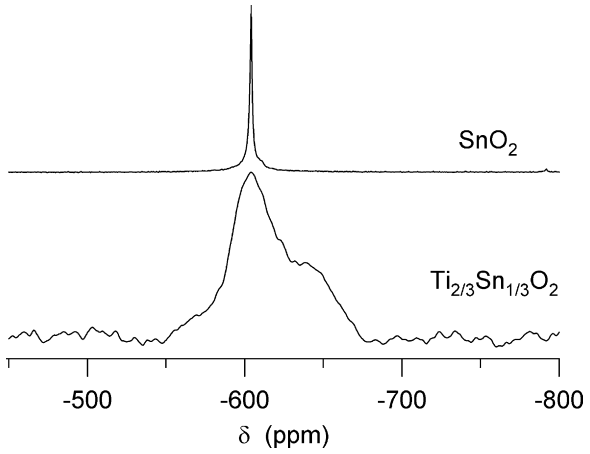

Fig. 7. ^{119}Sn MAS NMR spectra of $Ti_{2/3}Sn_{1/3}O_2$ and SnO_2.

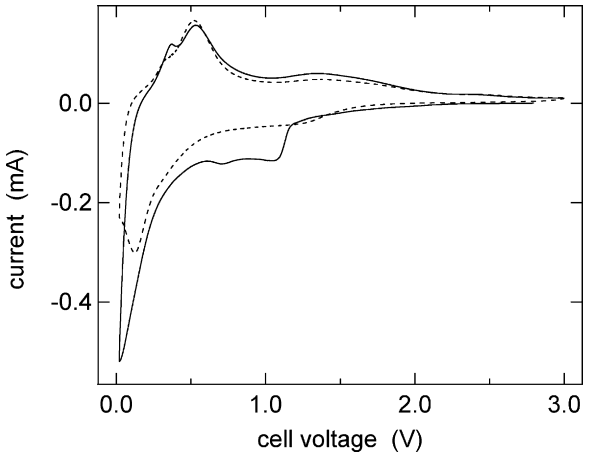

Fig. 9. Cyclic voltammogram of $Ti_{2/3}Sn_{1/3}O_2$ vs. Li|Li$^+$ during first cycle (solid line) and second cycle (dashed line) at a sweep rate of 0.05 mV s^{-1}.

of 5.8 mA g^{-1}. The shape of the voltage profile is very similar to that of pure SnO_2 [5]. More than 3.5 Li ions can be inserted per formula unit during the first discharge. The irreversible capacity in the first cycle is 440 mAh g^{-1}. During the following cycles almost 2 Li ions can be inserted/removed with high reversibility corresponding to a specific capacity of about 500 mAh g^{-1}.

In order to get more insight into the reaction mechanism that occurs during Li insertion, we acquired cyclic voltammograms and performed XRD measurements on electrodes after galvanostatic insertion/removal of different amounts of Li. The shape of the CV curve (Fig. 9.) is very similar to that of pure SnO_2 [6] and the main electrochemical activity occurs in the region between 0 V and 1 V. Only minor contributions are visible in the range from 1.5 V to 1.8 V, where $Ti^{3+/4+}$ is active. The XRD patterns obtained on samples after discharging to 1.15 V, 0.75 V, and 0.02 V (Fig. 10) reveal that the rutile/cassiterite structure disappears successively, and new peaks in the region between 20° and 25° 2θ appear. The peaks at 22.1°, 22.4°, and 22.8° can be assigned to $Li_{22}Sn_5/Li_5Sn_2$, $Li_{13}Sn_5$, and Li_7Sn_2, respectively. After recharging, these peaks disappear and only very broad contributions are visible in the pattern, hinting at a highly disordered structure. A broad peak around 45° 2θ might represent very small Sn metal particles. Metallic Ti cannot be detected in either of the patterns. If we assume that only Sn is active and that every Sn atom is able to accommodate 4.4 Li ions (resulting in a final alloy composition $Li_{22}Sn_5$), one formula unit of $Ti_{2/3}Sn_{1/3}O_2$ should be able to convert 1.46 Li ions which would correspond to a specific discharge capacity of 378 mAh g^{-1}. This value is very close to the experimental value obtained in the first cycles (cf. Fig. 8).

The specific charge and discharge capacities for the first 100 cycles are shown in Fig. 11. They show a slight decrease with about 300 mAh g^{-1} in the 100th cycle. The coulombic efficiency, i.e. the ratio of the charge capacity to the discharge capacity of each cycle, is shown in Fig. 12. Values close to 1 are obtained again reflecting the very high reversibility of the underlying reactions. The capacity losses occur mainly during discharging, i.e. during reduction of $Ti_{2/3}Sn_{1/3}O_2$ (see also Fig. 8).

Faster cycling with rates up to 20*C* lead to a drastic decrease of the specific capacities (Fig. 13). But when returning to slower

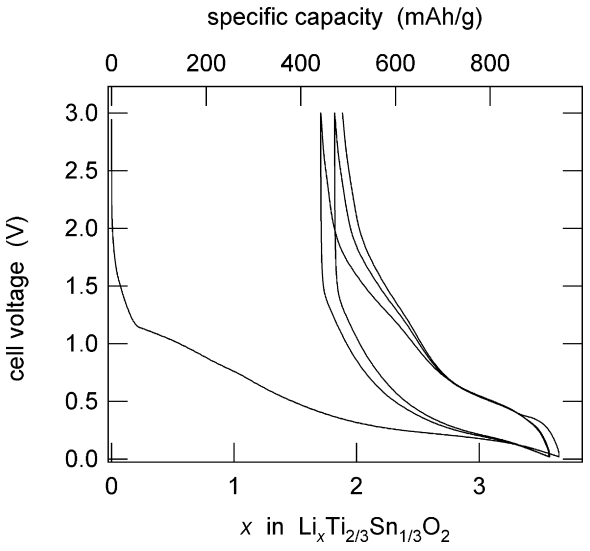

Fig. 8. The voltage as a function of Li content *x* (lower abscissa) and the corresponding specific capacity (upper abscissa) of $Li_xTi_{2/3}Sn_{1/3}O_2$ for the first three galvanostatic cycles at a rate of *C*/20.

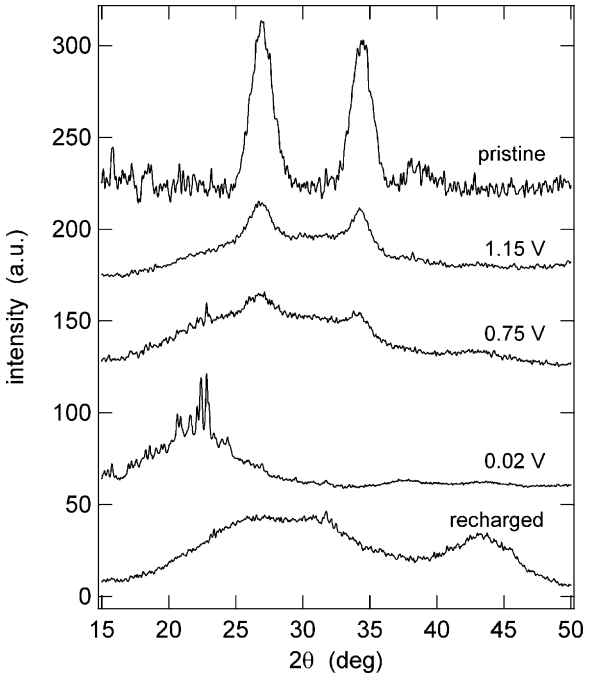

Fig. 10. XRD patterns of pristine $Ti_{2/3}Sn_{1/3}O_2$, after discharging to different voltages, and after one complete cycle.

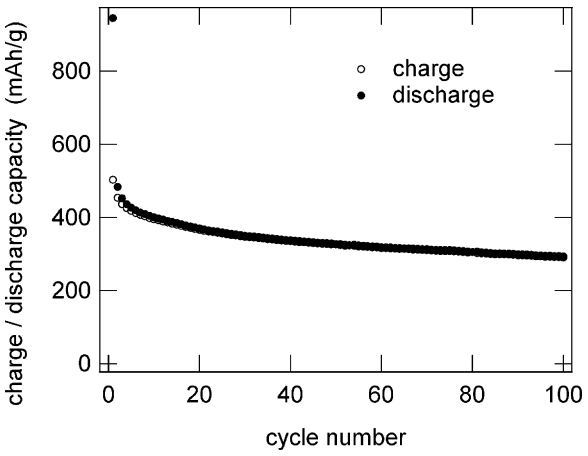

Fig. 11. The specific charge and discharge capacities for $Ti_{2/3}Sn_{1/3}O_2$ cycled against Li metal with *C*/20.

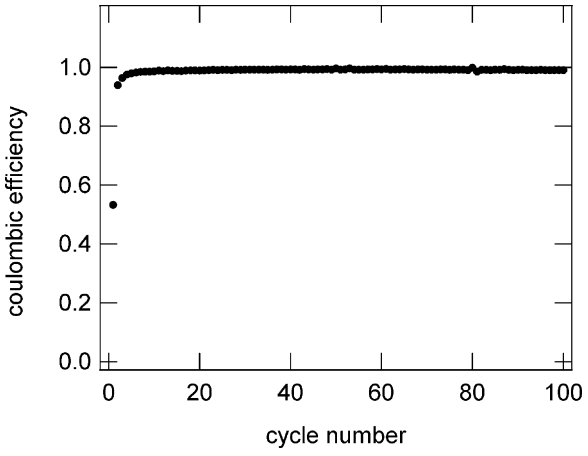

Fig. 12. The coulombic efficiency for $Ti_{2/3}Sn_{1/3}O_2$ cycled against Li metal with *C*/20.

cycling (*C*/20) the initial values with specific capacities of more than 400 mAh g^{-1} are obtained again.

In summary, our results show that $Ti_{2/3}Sn_{1/3}O_2$ shows good performance in terms of specific discharge capacity, cyclic stability, and low redox potential. The synthesis method offers the advantages of low cost and facile up-scaling.

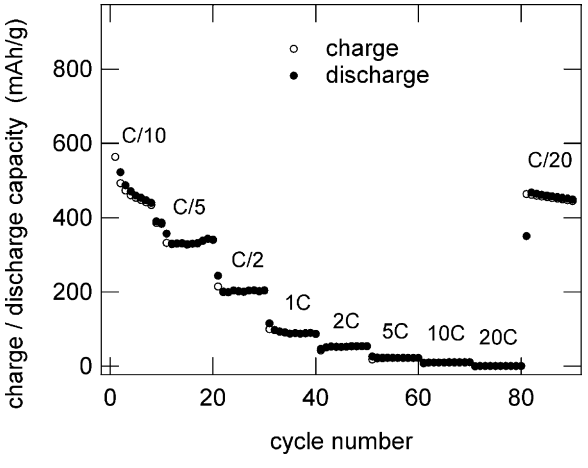

Fig. 13. The specific charge and discharge capacities for $Ti_{2/3}Sn_{1/3}O_2$ cycled against Li metal with different *C* rates.

4. Conclusion

We prepared nanocrystalline $Ti_{2/3}Sn_{1/3}O_2$ with a narrow crystallite size distribution around 5 nm. The synthesis method is inexpensive and offers the possibility of facile up-scaling. The existence of a solid solution was verified by XRD, STEM in combination with EDX, and NMR spectroscopy. Li could be inserted reversibly at a rate of *C*/20 with specific capacities of more than 300 mAh g^{-1} for 100 cycles. The shape of the voltage profile, cyclic voltammograms, and XRD measurements after complete Li insertion reveal that the electrochemical mechanism is similar to that of pure SnO_2.

Acknowledgements

We are grateful to the German Federal Ministry of Education and Research for financial support.

References

[1] D. Linden, T.B. Reddy (Eds.), Handbook of Batteries, McGraw-Hill, New York, 1995.
[2] W.A. van Schalkwijk, B. Scrosati (Eds.), Advances in Lithium-Ion Batteries, Kluwer Academic, New York, 2002.
[3] G.-A. Nazri, G. Pistoja (Eds.), Lithium Batteries: Science and Technology, Kluwer Academic, Boston, 2004.
[4] R.A. Huggins (Ed.), Advanced Batteries, Springer, New York, 2009.
[5] I.A. Courtney, J.R. Dahn, J. Electrochem. Soc. 144 (1997) 2045.
[6] J.L. Tirado, Mater. Sci. Eng. R 40 (2003) 103.
[7] R.A. Huggins, J. Power Sources 81–82 (1999) 13.
[8] N. Li, C.R. Martin, B. Scrosati, Electrochem. Solid-State Lett. 3 (2000) 316.
[9] C. Kim, M. Noh, M. Choi, J. Cho, B. Park, Chem. Mater. 17 (2005) 3297.
[10] H.-J. Ahn, H.-C. Choi, K.-W. Park, S.-B. Kim, Y.-E. Sung, J. Phys. Chem. B 108 (2004) 9815.
[11] A. Chandra Bose, D. Kalpana, P. Thangadurai, S. Ramasamy, J. Power Sources 107 (2002) 138.
[12] Y. Liang, J. Fan, X. Xia, Z. Jia, Mater. Lett. 61 (2007) 4370.
[13] Q.-H. Wu, J. Song, J. Kang, Q.F. Dong, S.-T. Wu, S.-G. Sun, Mater. Lett. 61 (2007) 3679.
[14] L. Yuan, Z.P. Guo, K. Konstantinov, H.K. Liu, S.X. Dou, J. Power Sources 159 (2006) 345.
[15] G.X. Wang, Y. Chen, L. Yang, J. Yao, S. Needham, H.K. Liu, J.H. Ahn, J. Power Sources 146 (2005) 487.
[16] C. Wang, Y. Zhou, M. Ge, X. Xu, Z. Zhang, J.Z. Jiang, J. Am. Chem. Soc. 132 (2010) 46.
[17] R. Alcántara, F.J. Fernández-Madrigal, C. Pérez-Vicente, J.L. Tirado, J.C. Jumas, J. Olivier-Fourcade, Chem. Mater. 12 (2000) 3044.
[18] R. Alcántara, G.F. Ortiz, J.L. Tirado, Chem. Phys. Chem. 8 (2007) 80.
[19] P.A. Connor, J.T.S. Irvine, J. Power Sources 97–98 (2001) 223.
[20] N. Sharma, K.M. Shaju, G.V. Subba Rao, B.V.R. Chowdari, J. Power Sources 139 (2005) 250.
[21] X. Hou, Q. Cheng, Y. Bai, W.F. Zhang, Solid State Ionics 181 (2010) 631.
[22] A. Rong, X.P. Gao, G.R. Li, T.Y. Yan, H.Y. Zhu, J.Q. Qu, D.Y. Song, J. Phys. Chem. B 110 (2006) 14754.
[23] X.J. Zhu, L.M. Geng, F.Q. Zhang, Y.X. Liu, L.B. Cheng, J. Power Sources 189 (2009) 828.
[24] Z. Yuan, F. Huang, J. Sun, Y. Zhou, J. Mater. Sci. Lett. 22 (2003) 143.
[25] S. Lei, K. Tang, C. Chen, Y. Jin, L. Zhou, Mater. Res. Bull. 44 (2009) 393.
[26] F. Huang, Z. Yuan, H. Zhan, Y. Zhou, J. Sun, Mater. Lett. 57 (2003) 3341.
[27] G. Wang, X.P. Gao, P.W. Shen, J. Power Sources 192 (2009) 719.
[28] H. Uchiyama, E. Hosono, H. Zhou, H. Imai, Solid State Ionics 180 (2009) 956.
[29] Y. Yu, L. Gu, C. Wang, A. Dhanabalan, P.V. van Aken, J. Maier, Angew. Chem. Int. Ed. 48 (2009) 6485.
[30] C.-M. Park, W.-S. Chang, H. Jung, J.-H. Kim, H.-J. Sohn, Electrochem. Commun. 11 (2009) 2165.
[31] S.Y. Huang, L. Kavan, I. Exnar, M. Grätzel, J. Electrochem. Soc. 142 (1995) L142.
[32] L. Kavan, M. Grätzel, J. Rathousky, A. Zukal, J. Electrochem. Soc. 143 (1996) 394.
[33] G. Sudant, E. Baudrin, D. Larcher, J.-M. Tarascon, J. Mater. Chem. 15 (2005) 1263.
[34] C. Jiang, M. Wei, Z. Qi, T. Kudo, I. Honma, H. Zhou, J. Power Sources 166 (2007) 239.
[35] P. Kubiak, J. Geserick, N. Hüsing, M. Wohlwahrt-Mehrens, J. Power Sources 175 (2008) 510.
[36] Y.-S. Hu, L. Kienle, Y.-G. Guo, J. Maier, Adv. Mater. 18 (2006) 1421.
[37] P. Kubiak, M. Pflanzelt, J. Geserick, U. Hörmann, N. Hüsing, U. Kaiser, M. Wohlfahrt-Mehrens, J. Power Sources 194 (2009) 1099.
[38] M. Pflanzelt, P. Kubiak, M. Wohlfahrt-Mehrens, Electrochem. Solid-State Lett. 13 (2010) A91.
[39] M. Zukalová, M. Kalbáč, L. Kavan, I. Exnar, M. Grätzel, Chem. Mater. 17 (2005) 1248.
[40] A.R. Armstrong, G. Armstrong, J. Canales, R. García, P.G. Bruce, Adv. Mater. 17 (2005) 862.

[41] A.R. Armstrong, G. Armstrong, J. Canales, P.G. Bruce, J. Power Sources 146 (2005) 501.
[42] L. Aldon, P. Kubiak, A. Picard, J.-C. Jumas, J.O. Fourcade, Chem. Mater. 18 (2006) 1401.
[43] N.J. Clayden, C.M. Dobson, A. Fern, J. Chem. Soc. Dalton Trans. 843 (1989).
[44] C. Cossement, J. Darville, J.-M. Gilles, J.B. Nagy, C. Fernandez, J.-P. Amoureux, Magn. Reson. Chem. 30 (1992) 263.
[45] R.H. Herber, Phys. Rev. B 27 (1983) 4013.
[46] M.S. Moreno, R.C. Mercader, Phys. Rev. B 50 (1994) 9875.
[47] A.L. Patterson, Phys. Rev. 56 (1939) 978.